

# **Nanoscale Organization of Junctophilin-2 and Ryanodine Receptors within Peripheral Couplings of Rat Ventricular Cardiomyocytes**

Izzy Jayasinghe,<sup>†‡</sup> David Baddeley,<sup>†</sup> Cherrie H. T. Kong,<sup>†</sup> Xander H. T. Wehrens,<sup>§</sup>  
Mark B. Cannell,<sup>†¶</sup> and Christian Soeller<sup>†</sup>

<sup>†</sup>Department of Physiology, School of Medical Sciences, University of Auckland, Auckland, New Zealand; <sup>‡</sup>School of Biomedical Sciences, University of Queensland, Brisbane, Australia; <sup>§</sup>Department of Molecular Physiology and Biophysics, Baylor College of Medicine, Houston, Texas; and <sup>¶</sup>Department of Physiology and Pharmacology, School of Medical Sciences, University of Bristol, Bristol, United Kingdom

## **Supplementary Information**

### **Methods**

#### **Sample preparation**

Rat ventricular cardiomyocytes were enzymatically isolated as described elsewhere (1), in accordance to the protocol approved by the University of Auckland Animal Ethics Committee. 250 g Wistar rats were euthanized by intraperitoneal injection of 100 mg/kg pentobarbitone. The heart was quickly dissected out and mounted by the aorta onto a Langendorff perfusion system. A 5 min perfusion with oxygenated  $\text{Ca}^{2+}$ -free Tyrode's solution at 37°C was followed by 10-15 min perfusion with the same solution containing 200  $\mu\text{M}$   $\text{CaCl}_2$ , 1.0 mg/ml Type II Collagenase (Worthington Biochemical, NJ) and 0.1 mg/ml Type I protease (Sigma-Aldrich, MO). Ventricles were then dissected, diced into smaller blocks and triturated within Tyrode's solution containing 200  $\mu\text{M}$   $\text{CaCl}_2$  to liberate single myocytes. The resulting suspension of cells was filtered and fixed in phosphate buffered saline (PBS) containing 2% paraformaldehyde (PFA; w/v; pH ~ 7.4) at room temperature (RT) for 12 minutes. Cells were then washed in fresh PBS for 10 min to remove residual PFA.

#### **Immunocytochemistry**

Fixed cells were incubated in PBS containing 1% Triton X-100 for 10 min at RT to permeabilize membranes prior to blocking with 10% goat serum (Vector Laboratories, Burlingame, CA). Ryanodine receptor-2 (RyR) and junctophilin-2 (JPH2) were labeled with a mouse monoclonal anti-RyR2 IgG (Thermo Scientific, Cat # MA3-916) and a polyclonal rabbit anti-JPH2 IgG raised against a synthetic peptide consisting of the amino acids 458-CRPRESPLQLHERETPQPEG-475 (2), respectively. Primary antibodies were incubated overnight at 4°C in an incubation buffer that contained 5% goat serum (Invitrogen, NZ), 1% bovine serum albumin (BSA; Gibco, NZ) and 0.05% Triton X-100. Samples were washed in fresh PBS three times for 10 minutes to remove excess antibody. Highly cross-adsorbed Alexa 680-linked goat anti-mouse IgG and Alexa 750-linked anti-rabbit IgG secondary antibodies (Invitrogen) were incubated for 2h at RT. Following three further washes, cells were transferred into a mounting medium containing 90% Glycerol (v/v), 10% PBS (v/v), 10% glucose (w/v), 5 mM  $\beta$ -mercaptoethylamine (Sigma-Aldrich), 0.5 mg/mL glucose oxidase (Sigma-Aldrich) and 40 mg/mL catalase (Sigma-Aldrich). This suspension of cells was mounted on a number 1.5 coverslip and its edges were sealed against the slide using nail varnish.

Samples prepared for comparative confocal imaging were labeled using the same protocol with Alexa 488 and Alexa 594-linked secondary antibodies (Invitrogen) instead of the near-infrared secondary antibodies. Cells were mounted onto a number 1.5 glass coverslip, immersed in a mounting medium containing glycerol and PVA (Sigma-Aldrich) to achieve a refractive index of ~1.51.

#### **Imaging setup for single molecule detection**

Images of fluorescence labeling near the surface of cells close to the coverslip were acquired using a Nikon 60x oil immersion 1.49NA TIRF objective (Nikon, Japan) mounted on a custom made objective holder directly coupled to a Nikon TE2000 inverted microscope. Samples were illuminated at ~200 mW using a solid state 671 nm laser focused onto a ~10  $\mu\text{m}$  wide area near the cell surface in a highly inclined light sheet. Emission light was separated from excitation light

using a Q680LP dichroic mirror (Chroma Technology) and passed through a custom made splitter device that separates this emission into two spectral channels split at 741 nm (3). The two channels were recorded onto top and bottom halves of 515×512 pixel 16-bit TIFF images using an Andor IXon DV887DCSBV electron multiplying CCD camera (Andor Technology, UK).

### **Image acquisition and single molecule event detection**

A series of ~20,000 frames was acquired at an integration time of 40-50 ms/frame. Single molecule events (that lasted up to a few frames) were detected (typical mean localization accuracy was ~13 nm using the fitting algorithm described previously (4)). Fig. S1A illustrates the positions of detected single molecule events in an image series acquired near the surface of a rat ventricular myocyte labeled with a mouse anti-RyR IgG primary antibody and an Alexa 680-linked goat anti-mouse IgG secondary antibody. Panel S1B shows the diffraction-limited widefield image of the corresponding region. Events in the two halves of the EM-CCD camera (corresponding to the two spectral channels separated by the second dichroic splitter) were detected simultaneously and classified according to the amplitudes in the two channels as Alexa 680 or Alexa 750 based on criteria that ensured that the probability of crosstalk was < 1%, as described (3).

### **Confocal imaging**

Z-stacks of longitudinal confocal optical sections near the surface of labeled myocytes were acquired using a LSM710 laser scanning confocal microscope (Zeiss, Jena, Germany) with a 63x 1.4NA oil immersion objective. Data volumes with a z-spacing of 0.2  $\mu\text{m}$  and in-plane x-y sampling of 0.5  $\mu\text{m}/\text{pixel}$ . Image volumes were deconvolved using a maximum-likelihood Richardson-Lucy algorithm described in (5). Deconvolved confocal images were binarized using a protocol based on maximum-entropy filtering described previously (6).

### **Co-localization analysis**

The event positions for each channel were rendered onto a 5 nm pixel grid to produce images using an algorithm based on Delaunay triangularization of the data as described previously (7) which converts the event data into an event density map. The resulting density images are essentially equivalent to conventional fluorescence images (albeit have much higher resolution) where local intensity reflects the density of marker molecules. The process is illustrated in Fig S1C which shows a rendered image generated from localized fluorophore positions shown in panel S1A.

To construct cluster masks for co-localization analysis regions containing labeling were binarized by grouping local areas of data points that were separated from surrounding points by a distance no larger than the effective resolution of the rendered image (i.e. ~30 nm), see (4) for details. In effect this corresponds to a threshold on event density, equivalent to thresholding applied to conventional fluorescence images in calculating co-localization (8). Fig S1 D shows the binary image corresponding to the single molecule events shown in panel A. Small gaps (typically 30-40 nm wide) appearing within binarized regions were most likely patches of incomplete labeling within the cluster. These regions were filled to generate the masks for co-localization analysis.

Co-localization was quantified by calculating distance maps of the distance to the edge of the respective cluster mask. Here we used the convention that distances within the cluster mask are counted negative, distances outside the mask are positive. Using the labeling in the channel of interest (e.g. JPH2) the fraction of labeling at given distances was calculated by using the distance

map from the other channel (e.g. the RyR cluster distance map). The fractions are summarized in distance histograms (as shown in Fig 2). The approach is similar to the analysis described in (6), the distance map construction is illustrated with super-resolution data in Fig. S1.

The resulting distance histograms are normalized so that total labeling sums to 100% (as shown in Figs. 2 and S2). The histograms include information that corresponds to the established Manders coefficients (9). These are obtained by summing all labeling at distances less or equal to zero thus quantifying the fraction of labeling in one channel (e.g. JPH) “overlapping” with labeling of the other channel (e.g. RyR). The criterion for presence of labeling in the other channel is based on the cluster mask which results from thresholding the label at a molecular density of 30 nm, as described above and in (4). In addition, the distance histograms allow the calculation of fractions that take into account uncertainties in determining the boundary of clusters and biological distances of interaction. To quantify the degree of co-clustering of JPH2 and RyRs we therefore also specify the co-localization obtained by including the labeling in a 30 nm band around the respective cluster masks (main text and Table S1). This is based on the idea that (a) 30 nm is comparable to the diameter of a single RyR and (b) 30 nm is approximately the resolution of our method, suggesting that here is at least a 30 nm uncertainty in determining the edges of clusters.

### **Density analysis of labeling within clusters**

To characterise the density of labeling within clusters we also performed a distance based density analysis of labeling. The approach is essentially the same as that to calculate density histograms as described above, up to the final analysis step where, instead of the total fractional labeling at a given distance, we estimated the average density of labeling at a distance from the cluster mask by calculating the ratio between the amount of labeling within the given distance band and the image area within the given distance band. We calculated both the density of RyR labeling as a function of distance to the edge of RyR clusters as well as the density of JPH2 labeling to the same RyR cluster edges. Comparison of the density-distance curves then allowed comparison of how differently RyRs and JPH2 are distributed across RyR clusters, as shown in Fig. S3.

### **Analysis of cluster alignment**

To quantify the alignment of patches we excised small regions of interest (ROIs) around identified clusters in both the JPH2 and RyR channels ( $n = 30$  clusters were analyzed in this way). The angular alignment between clusters was calculated by computing Pearson’s correlation coefficient between the original RyR cluster and a rotated copy of the corresponding ROI in the JPH2 channel as a function of the rotation angle. Mean and standard errors of the correlation coefficients as a function of angle were determined and displayed in a polar plot.

The correlation between aligned JPH2 and RyR clusters was on average  $\sim 0.6$  (Fig. 3B). To calculate the expected peak correlation between perfectly aligned structures we also calculated Pearson’s correlation coefficient between the recorded RyR cluster data and a random subsampled fraction of the RyR event data (reflecting the fact that the density of JPH2 events was typically slightly lower than the RyR event density, partly because of differences in fluorochrome behavior and possibly antibody affinity). The analysis of correlation between this RyR data and its subsampled copy resulted in a mean correlation of  $0.76 \pm 0.03$  (std. dev.,  $n = 4$  images). This showed that the mean correlation for, in principle, identical structures is considerably lower than the theoretical maximum (i.e. 1) due to stochastic variations in single molecule localization.

Similarly, the translational alignment between corresponding clusters was determined by calculating the center of intensity coordinates in the RyR and JPH2 channels of the ROIs, respectively. The distance between cluster centroids in the RyR and JPH was calculated and displayed, see Fig. 3.

## References

1. Evans, A. M., and M. B. Cannell. 1997. The role of L-type  $\text{Ca}^{2+}$  current and  $\text{Na}^{+}$  current-stimulated Na/Ca exchange in triggering SR calcium release in guinea-pig cardiac ventricular myocytes. *Cardiovasc Res.* 35:294-302.
2. van Oort, R. J., A. Garbino, W. Wang, S. S. Dixit, A. P. Landstrom, N. Gaur, A. C. De Almeida, D. G. Skapura, Y. Rudy, A. R. Burns, M. J. Ackerman, and X. H. Wehrens. 2011. Disrupted Junctional Membrane Complexes and Hyperactive Ryanodine Receptors After Acute Junctophilin Knockdown in Mice. *Circulation* 123:979-988.
3. Baddeley, D., D. Crossman, S. Rossberger, J. E. Cheyne, J. M. Montgomery, I. Jayasinghe, C. Cremer, M. B. Cannell, and C. Soeller. 2011. 4D Super-Resolution Microscopy with Conventional Fluorophores and Single Wavelength Excitation in Optically Thick Cells and Tissues. *PLoS ONE* 6:e20645.
4. Baddeley, D., I. Jayasinghe, L. Lam, S. Rossberger, M. B. Cannell, and C. Soeller. 2009. Optical single-channel resolution imaging of the ryanodine receptor distribution in rat cardiac myocytes. *Proc Natl Acad Sci U S A* 106:22275-22280.
5. Soeller, C., and M. B. Cannell. 1999. Examination of the transverse-tubular system in living cardiac rat myocytes by 2-photon microscopy and digital image-processing techniques. *Circ Res.* 84:266-275.
6. Jayasinghe, I., M. B. Cannell, and C. Soeller. 2009. Organization of ryanodine receptors, transverse tubules and sodium-calcium exchanger in rat myocytes. *Biophys. J.* 97:2664-2673.
7. Baddeley, D., M. B. Cannell, and C. Soeller. 2010. Visualization of localization microscopy data. *Microscopy Microanalysis* 16:64-72.
8. Scriven, D. R. L., P. Dan, and D. W. Moore. 2000. Distribution of Proteins Implicated in Excitation-Contraction Coupling in Rat Ventricular Myocytes. *Biophys. J.* 79:2682-2691.
9. Manders, E. M. M., F. J. Verbeek, and J. A. Aten. 1993. Measurement of co-localization of objects in dual-colour confocal images. *J Microsc.* 169:375-382.

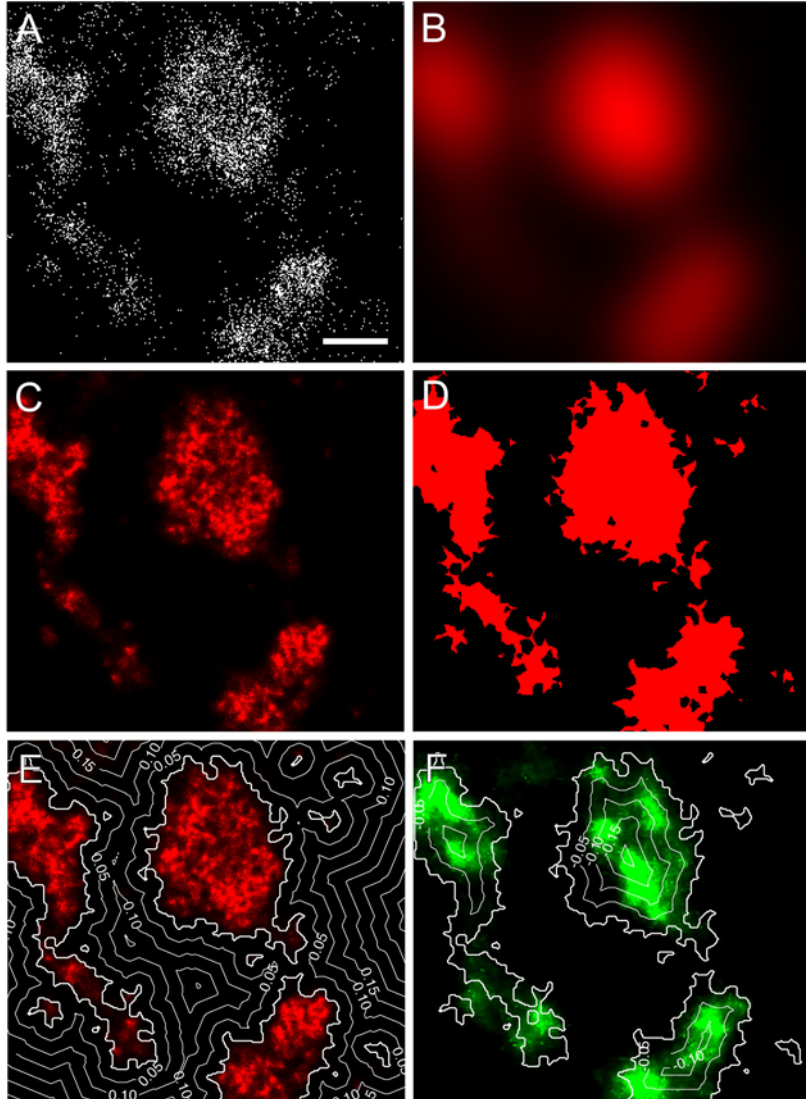


Figure S1: Visualization and analysis of single molecular localization data. A) The positions of individual events detected over a  $\sim 20,000$  frame data series acquired near the surface of a myocyte labeled for RyR are shown as white points. Scale bar:  $0.25 \mu\text{m}$ . B) The diffraction-limited corresponding widefield image generated from the data. C) The intensity image generated from the point data that reflects the local event densities. D) The binary mask generated from the density image shown in C. E) The binary mask was used to generate distance contours that quantify the distance to the nearest cluster edge, here shown overlaid with the original density data (see C). F) To quantify colocalization these contours were overlaid on the other channel (here shown in green) and we calculated the fraction of labeling in this channel as a function of distance to cluster edges. Note that distances within the cluster boundaries were counted as negative values. The quantification of fractional labeling into these “distance bands” was used to generate distance histograms. The total co-localizing fraction can be calculated by determining the fraction of labeling with zero or negative distances, i.e. the fraction within the mask shown in D. Distances shown on contours are labeled in micron.

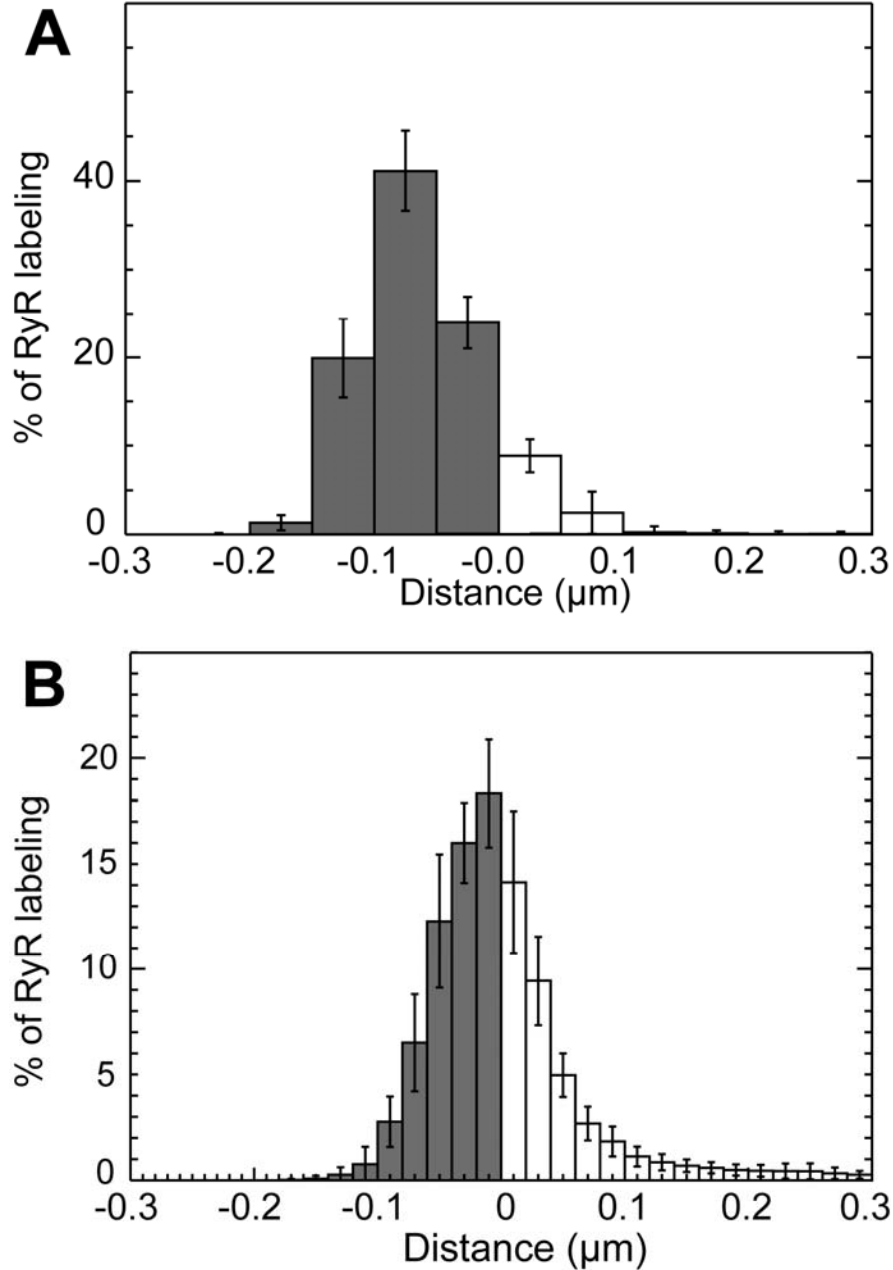


Figure S2: Quantification of co-localization of RyRs with JPH2. A) The histogram shows the total percentage of RyR labeling in confocal images as a function of the distance to the edge of the nearest region of JPH labeling. The shaded bars correspond to the fraction of RyR labeling that was detected within the JPH mask ( $86.1 \pm 2.8\%$  for confocal data;  $n = 5$  cells) B) An equivalent analysis performed on localization data is shown in the histogram.  $57.2 \pm 3.6\%$  of the RyR labeling in the localization images was co-localized with JPH ( $n = 5$  cells) which increases to  $\sim 81\%$  within a distance corresponding to one RyR diameter ( $\sim 30$  nm).

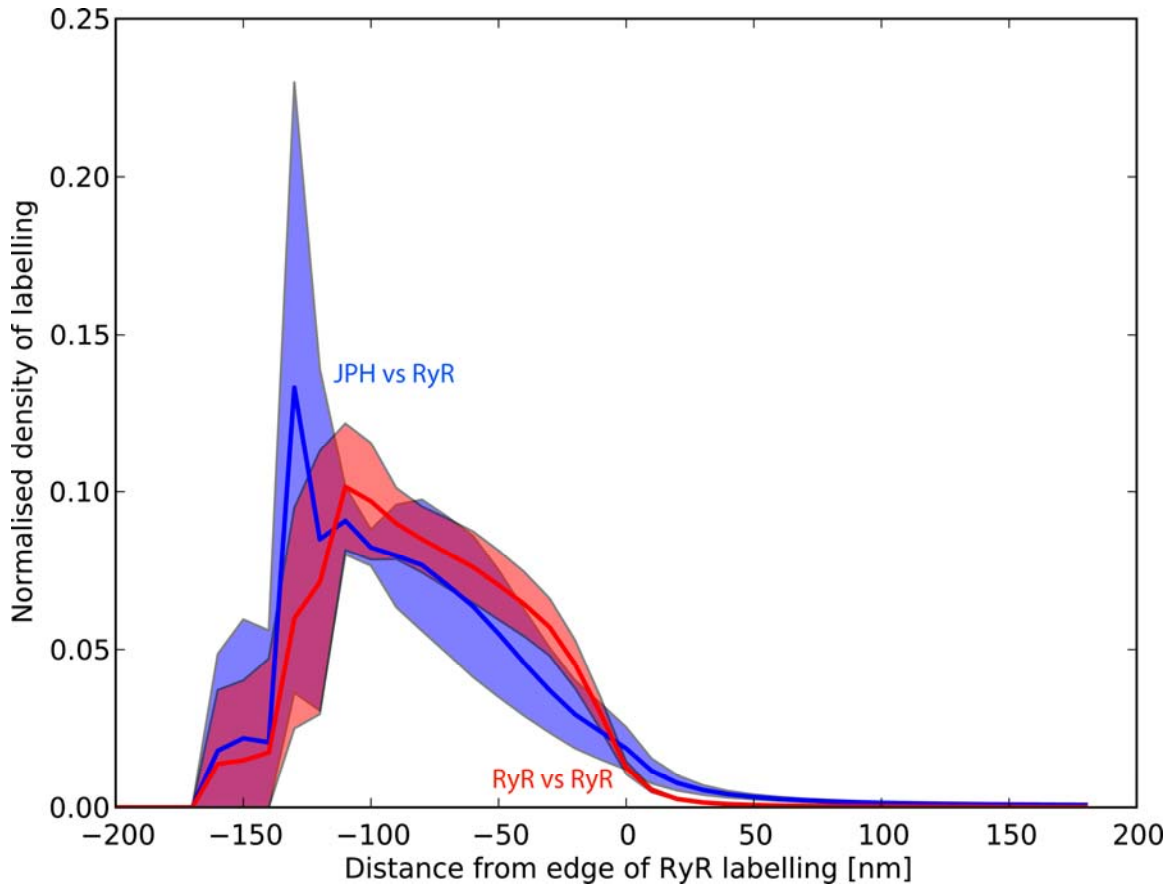


Figure S3: Density of labeling with distance to the edge of RyR labeling. The density is shown both for the RyR labeling (red) and the JPH labeling, both with respect to the RyR labeling cluster mask. The shaded bands show the variation in density (standard deviation) indicating that density estimates at more negative distances (i.e. deep within the cluster mask) are associated with larger errors due to the small area sampled, i.e. the low number of “very large” clusters. It is notable that the RyR density (with respect to the RyR cluster mask itself) is relatively flat within clusters but gradually decays towards the cluster edge (and decays sharply at the edge itself). This is not surprising since a lower density of RyR label defines the edges of the cluster in the first place. The JPH density, by comparison, shows a very similar tendency and decays with a similar slope towards the RyR cluster edge. In other words, the JPH distribution is very similar across RyR clusters to the RyR label distribution itself, although, outside of RyR clusters, there is a crossover and the density of JPH labeling is slightly higher corresponding to a small component of JPH located outside RyR clusters but mostly in the immediate vicinity of the cluster edge ( $\leq 50$  nm).

	% of JPH co-localizing with RyR	% of RyR co-localizing with JPH	n (cells)	n (animals)
Confocal microscopy	86.6 ± 2.2	83.6 ± 2.9	5	3
Super-res microscopy	72.0 ± 2.5	57.2 ± 3.6	5	2
Super-res microscopy, within 30 nm of cluster boundary	90.4 ± 0.5	80.6 ± 3.1	5	2

Table S1: Summary of percentages of co-localization between JPH and RyR from confocal and super-resolution microscopy data (Mean ± SEM). Also shown are generalized co-localizing fractions that include the staining in a band ~ one RyR wide (~30 nm) around the cluster edges of JPH/RyRs.